THE AMERICAN SOCIETY OF MECHANICAL ENGINEERS
345 E. 47th St., New York, N.Y. 10017

97-GT-295

IVERSE DESIGN OF TURBOMACHINERY BLADING FOR ARBITRARY BLADE THICKNESS IN THREE-DIMENSIONAL TRANSONIC FLOW

Y. L. Yang
Chung-Hua Polytechnic Institute
Department of Mechanical Engineering
Hsin Chu, Taiwan 308
R.O.C.

ABSTRACT

A three-dimensional inverse design of turbomachinery blading for arbitrary blade thickness was obtained by using two periodic bound vortex sheets representing the pressure side and suction side of a blade row. The mean swirl distribution and blade tangential thickness distribution are specified in the present inverse design method. The prescribed mean swirl distribution is split into two fractions to form the strength of two bound vortex sheets. However, the designed results are uniquely determined by the specification of the mean swirl distribution and blade tangential thickness distribution, while splitting the mean swirl distribution into any two fractions for two bound vortex sheets is irrelevant. The resulting velocity field is composed of three parts: the first is sawtooth integrated from two bound vortex sheets; the second is axisymmetrical to provide an irrotational flow outside the two bound vortex sheets; and the last is potential to ensure mass conservation. The blade shape is determined from either the pressure side or suction side boundary condition, without a difference. Numerical results of a subsonic stator blade row designed by the present inverse design have been compared with three-dimensional Euler solutions and show a good agreement. For transonic calculation, a special form of retarding density was implemented to avoid transformation of the coordinate. However, due to the nonisentropic and rotational nature of shock wave, the present inverse solution does not give a correct answer after shocks. Coupling the entropy change and generation of vorticity after shocks with the present analytical formulation is recommended in the future work.

NOMENCLATURE

C_p = specific heat at constant pressure
n = number of blades
f = blade wrap angle, Eq. (2)
$\bar{f}$ = blade mean wrap angle
$\bar{g}$ = grid directional vector
I = rothalpy
$S(\alpha)$ = sawtooth function, Eq. (6)
$\bar{s}$ = local flow direction
T_1 = periodic step function, Eq. (18)
T_2 = periodic step function, Eq. (19)
t = splitting function
$\bar{W}$ = relative velocity
$\bar{W}^*$ = velocity from the sum of mean flow part and sawtooth part
α = blade surface, Eq. (2)
$\delta_p(\alpha)$ = periodic delta function, Eq. (4)
Δf = blade tangential thickness
ν = coefficient of retarding density, Eq. (13)
$\bar{\Omega}$ = vorticity
ω = blade rotational speed
Φ = velocity potential
Ψ = Stokes stream function

Subscripts

r,θ,z = the $r-,\theta-,z-$ component
s/p = the blade suction/pressure surface
∞ = upstream

INTRODUCTION

In the two papers on the "Theory of Blade Design for Large Deflections" published by Hawthorne et al. (1984) and Tan et al. (1984), a new technique was presented for designing the shape of turbomachinery blades in three-dimensional flow. Several researchers such as Hawthorne and Tan (1987), Ghaly (1990), Borges (1990a), Zangeneh (1991), and Yang et al. (1993) applied this theory to design radial inflow turbines. The experimental data reported by Borges (1990b) and Zangeneh (1990) showed that the radial inflow turbines designed by this technique gave an improvement in efficiency over a wide operating range. Dang (1993) used a finite-volume technique to

Presented at the International Gas Turbine & Aeroengine Congress & Exhibition
Orlando, Florida — June 2–June 5, 1997

solve the relevant equations in the conservative forms and extended the design technique to transonic flow regimes successfully. Zangeneh (1994) combined the inverse design with viscous calculation to avoid flow separation and secondary motion in a centrifugal compressor. Recently, Dang and Isgro (1995) coupled the inverse design idea with an Euler time-marching solver to deal with rotational flow and complex shock structures in designed cascades. To avoid the reverse flow on a highly loaded radial inflow turbine by using splitter blades, Tjokroaminata et al. (1996) developed a two-vortex-sheet formulation to represent main blades and splitter blades. Besides, Zangeneh (1996) extended the inverse design to handle inlet shear flow for centrifugal vaned diffusers.

The above inverse design technique using a single bound vortex sheet formulation (see Fig. 1a) has assumed the blades to be infinitely thin. In this paper, an extension of the theory to design three-dimensional turbomachinery blading for arbitrary blade thickness is introduced. The utilization of a splitting function to formulate two periodic bound vortex sheets allows the correct treatment of blade thickness. A detail derivation is given and three-dimensional calculations are used to demonstrate the applications of the present technique.

Additionally, a different approach from Dang (1993) and Dang and Isgro (1995) is proposed to solve the inverse problems in transonic flow. The classical upwinding of the density is applied here (Jameson, 1975, Holst and Ballhaus, 1979). The retarding density introduces artificial viscosity implicitly to maintain stability in supersonic zones. The advantage of modifying the density is that this permits the algorithm for solving the discretised equations to be implemented more easily and maintains the same two bound vortex sheets' formulation. Numerical comparisons of transonic inverse design results with corresponding Euler solutions show the current approach is robust and well suited to design blades for transonic compressors.

THEORETICAL FORMULATION

A useful design specification for the inverse design of blading in three-dimensional flow is the mean swirl distribution $r\bar{V}_\theta$ (Tan et al., 1984); it is given by:

$$r\bar{V}_\theta(r,z)=\frac{n}{2\pi}\int_f^{f+2\pi/n} rV_\theta(r,\theta,z)d\theta \qquad (1a)$$

where the overbar defines a tangential mean, n is the number of blades, f is the angular coordinate of a point on the blade surface (see Fig. 1a) and (r,θ,z) is the usual right-handed cylindrical coordinate system. As $2\pi r\bar{V}_\theta$ is the circulation around the axis, this technique is the so called circulation method (Hawthorne and Tan, 1987). This scheme has been used in infinitely thin blade design successfully. From an aerodynamic viewpoint, it is quite natural to use two bound vortex sheets to represent the two sides of a blade when blade thickness effect is taken into account. Under this consideration, the definition of mean swirl distribution defined within the blade-to-blade plane , i.e., from pressure surface to suction surface, is modified to

$$r\bar{V}_\theta(r,z)=\frac{1}{(f_p+2\pi/n-f_s)}\int_{f_s}^{f_p+2\pi/n} rV_\theta(r,\theta,z)d\theta \qquad (1b)$$

where the subscripts s and p represent the blade suction side and pressure side respectively (see Fig. 1b).

The principal idea in this newly extended inverse design method is to split the mean swirl distribution $r\bar{V}_\theta$ into two fractions to formulate the strength of two vortex sheets, one fraction for the blade suction surface $tr\bar{V}_\theta$ and one for the blade pressure surface $(1-t)r\bar{V}_\theta$. In the later text, we will show that the splitting distribution $t(r,z)$ has no influence on the solution and can be picked arbitrarily (except 0 and 1 which provide a single vortex sheet). A general expression of suction side and pressure side blade surfaces is given by

$$\alpha_s(r,\theta,z)=\theta-f_s(r,z)=\pm\frac{2\pi k}{n}$$
$$\alpha_p(r,\theta,z)=\theta-f_p(r,z)=\pm\frac{2\pi k}{n} \qquad (2)$$
$$\text{for } k=0,1,2,3,\ldots,(n-1)$$

where k is an integer. It is convenient to use the blade tangential thickness, $\Delta f=f_s-f_p$, as an input for inverse design problems and solve for blade mean wrap angle, i.e., $\bar{f}=(f_p+f_s)/2$.

If the flow is steady, i.e., the approaching upstream flow is axisymmetric, irrotational, and reversible (hence, a homenthalpic and homentropic flow), then the absolute vorticity $\vec{\Omega}$ bound to the blades can be written as

$$\vec{\Omega}=(\nabla(tr\bar{V}_\theta)\times\nabla\alpha_s)\delta_p(\alpha_s)+(\nabla((1-t)r\bar{V}_\theta)\times\nabla\alpha_p)\delta_p(\alpha_p) \qquad (3)$$

where $\delta_p(\alpha)$ is the periodic delta function (Lighthill, 1958), given as

$$\delta_p(\alpha)=\frac{2\pi}{n}\sum_{k=-\infty}^{\infty}\delta(\alpha-\frac{2\pi k}{n})=\sum_{k=-\infty}^{\infty}e^{ikn\alpha} \qquad (4)$$

The solution for equation (3) is given by Clebsch's transformation (Lamb, 1932), i.e.,

$$\vec{V}=\nabla\Phi+tr\bar{V}_\theta\nabla\alpha_s-S(\alpha_s)\nabla(tr\bar{V}_\theta)$$
$$+(1-t)r\bar{V}_\theta\nabla\alpha_p-S(\alpha_p)\nabla((1-t)r\bar{V}_\theta) \qquad (5)$$

where $S(\alpha)$ is the periodic sawtooth function (Lighthill, 1958) shown in Fig. 2a, given as

$$S(\alpha)=\sum_{k=-\infty}^{\infty}\frac{e^{ikn\alpha}}{ikn} \qquad (6)$$

When solving, it is more convenient if the velocity in Eq. (5) is rearranged into the sum of a potential part, a mean flow part and a sawtooth part, as

$$\vec{W}=\nabla\Phi+\langle\bar{V}_r,\bar{V}_\theta-r\omega,\bar{V}_z\rangle$$
$$-S(\alpha_s)\nabla(tr\bar{V}_\theta)-S(\alpha_p)\nabla((1-t)r\bar{V}_\theta)=\nabla\Phi+\vec{W}^* \qquad (7)$$

where ω is blade rotational speed and $\vec{W}^*$ represents the velocity from the sum of mean flow part and sawtooth part.

We can use the Stokes stream function ψ to reduce the mean flow variables into a scalar, i.e..

$$V_r = -\frac{1}{r}\frac{\partial \psi}{\partial z}$$
$$V_z = \frac{1}{r}\frac{\partial \psi}{\partial r} \tag{8}$$

By taking the curl of Eq. (7) and comparing it with Eq. (3), the requirement of zero tangential vorticity outside the bound vortex sheet is

$$\frac{\partial V_r}{\partial z} - \frac{\partial V_z}{\partial r} = \frac{\partial r\bar{V}_\theta}{\partial r}\frac{\partial f_s}{\partial z} - \frac{\partial r\bar{V}_\theta}{\partial z}\frac{\partial f_s}{\partial r} + \frac{\partial (1-t)r\bar{V}_\theta}{\partial r}\frac{\partial f_p}{\partial z} - \frac{\partial (1-t)r\bar{V}_\theta}{\partial z}\frac{\partial f_p}{\partial r} \tag{9}$$

Combining Eq. (8) and (9), the governing equation for ψ can be written as

$$\frac{\partial^2 \psi}{\partial r^2} - \frac{1}{r}\frac{\partial \psi}{\partial r} + \frac{\partial^2 \psi}{\partial z^2} = r\left\{\frac{\partial r\bar{V}_\theta}{\partial z}\frac{\partial f_s}{\partial r} - \frac{\partial r\bar{V}_\theta}{\partial r}\frac{\partial f_s}{\partial z} + \frac{\partial (1-t)r\bar{V}_\theta}{\partial z}\frac{\partial f_p}{\partial r} - \frac{\partial (1-t)r\bar{V}_\theta}{\partial r}\frac{\partial f_p}{\partial z}\right\} \tag{10a}$$

The right hand side of Eq. (10a) can be simplified further by introducing the specification of blade tangential thickness as

$$\frac{\partial^2 \psi}{\partial r^2} - \frac{1}{r}\frac{\partial \psi}{\partial r} + \frac{\partial^2 \psi}{\partial z^2} = r\left\{\frac{\partial r\bar{V}_\theta}{\partial z}\frac{\partial f}{\partial r} - \frac{\partial r\bar{V}_\theta}{\partial r}\frac{\partial f}{\partial z} + \frac{1}{2}\left[\frac{\partial r\bar{V}_\theta}{\partial z} - \frac{\partial (1-t)r\bar{V}_\theta}{\partial z}\right]\frac{\partial \Delta f}{\partial r} - \frac{1}{2}\left[\frac{\partial r\bar{V}_\theta}{\partial r} - \frac{\partial (1-t)r\bar{V}_\theta}{\partial r}\right]\frac{\partial \Delta f}{\partial z}\right\} \tag{10b}$$

It is clear that Eq. (10b) is identical to Eq. (28) in Tan et al. (1984) when there is no blade thickness, i.e., $\Delta f(r,z) = 0$.

From the mass conservation, the governing equation for velocity potential Φ is

$$\nabla \bullet (\rho \nabla \Phi) = -\nabla \bullet (\rho \vec{W}^*) \tag{11}$$

For homenthalpic and homentropic flow, the density ρ can be computed from

$$\frac{\rho}{\rho_\infty} = \left\{\frac{I + 0.5\omega^2 r^2 - 0.5W^2}{C_p T_\infty}\right\}^{\frac{1}{\gamma - 1}} \tag{12}$$

where I is the rothalpy, C_p is the specific heat at constant pressure, and γ is the ratio of specific heat. The above scheme has been successfully applied to subsonic flow design. For transonic flows, an effective switch to an upwind difference scheme in the supersonic region is accomplished by adding an artificial viscosity. Following the work by Holst and Ballhaus (1979), a retarding density ρ^* is used in Eq. (11) to provide an effective artificial viscosity implicitly. If the ξ-direction is the local flow direction, then

$$\rho_i^* = (1-\nu)\rho_i + \nu \rho_{i-1} \tag{13}$$

where $\nu = \max\{0, (1 - 1/M^2)\}$ and M is the local Mach number. Since the computational grid may not coincide with the local flow direction, the upstream density ρ_{i-1} in Eq. (13) is approximated by

$$\rho_{i-1} \cong \rho_{i,j,k} + \frac{((\rho_{i-1,j,k} - \rho_{i,j,k})\bar{g}_\xi \cdot \bar{s} + (\rho_{i,j-1,k} - \rho_{i,j,k})\bar{g}_\eta \cdot \bar{s} + (\rho_{i,j,k-1} - \rho_{i,j,k})\bar{g}_\varsigma \cdot \bar{s})}{\sqrt{(\bar{g}_\xi \cdot \bar{s})^2 + (\bar{g}_\eta \cdot \bar{s})^2 + (\bar{g}_\varsigma \cdot \bar{s})^2}} \tag{14}$$

where $\bar{S}$ is the unit vector of local flow direction. $\bar{g}_\xi$ is the grid directional vector defined as $\bar{g}_\xi = <x_{i-1,j,k} - x_{i,j,k}, y_{i-1,j,k} - y_{i,j,k}, z_{i-1,j,k} - z_{i,j,k}>$, and the definitions of $\bar{g}_\eta$ and $\bar{g}_\varsigma$ are similar. In Eq. (14), the flow direction is assumed to be positive in ξ, η ,and ς directions.

Now, the only unknown remaining in this derivation is the blade wrap angle. For a given blade tangential thickness distribution, the blade wrap angle can be determined from either the suction side or pressure side inviscid boundary condition. When the blade is highly loaded, the pressure surface may have regions of "inviscid reverse flow;" hence to avoid numerical difficulty, using the suction side boundary condition is preferred. The condition of no normal velocity on the blade suction surface yields

$$\vec{W}_s \bullet \nabla \alpha_s = 0 \tag{15a}$$

where subscript S denotes flow variables on suction surface. Expanding Eq. (15a), the blade mean wrap angle can be computed by

$$(W_r)_s \frac{\partial \tilde{f}}{\partial r} + (W_z)_s \frac{\partial \tilde{f}}{\partial z} = \frac{(W_\theta)_s}{r} - \frac{1}{2}\left\{(W_r)_s \frac{\partial \Delta f}{\partial r} + (W_z)_s \frac{\partial \Delta f}{\partial z}\right\} \tag{15b}$$

Given the distribution of mean swirl $r\bar{V}_\theta$ and blade tangential thickness Δf, the procedure for determining the blade shape is an iterative one (Tan et al., 1984; Hawthorne and Tan 1987; Yang et al., 1993; Tjokroaminata, 1996). A first guess for the blade shape is used to generate a three-dimensional computational grid and compute the mean flow velocities from Eq. (10b); then density is obtained from Eq. (12) and (13); then the full-potential equation with a source term, Eq. (11), is solved; and finally the blade mean wrap angle is updated by using the blade boundary condition of Eq. (15). The iteration goes on until blade shape is converged.

NUMERICAL TECHNIQUE

In this section, the numerical technique used to solve the relevant equations described in the previous section will be presented. There are three partial differential equations encountered in the iterative scheme which are: (1) the governing equation for the Stokes stream function ψ, (2) the governing equation for the potential function Φ, and (3) the governing equation for the blade mean wrap angle $\tilde{f}$. Additionally, the grid system used in the present study is described.

Stokes Stream Function Solver. The requirement for vanishing tangential vorticity outside the blade gives the governing equation for the Stokes stream function, i.e., Eq. (10b). This second order partial differential equation is solved by a standard 2-D Galerkin finite element method (Ghaly, 1990). Along the inflow section, $\psi_{-\infty}$ is given. Along the outflow section, parallel flow is assumed ($\partial \psi / \partial n = 0$). For hub and shroud boundaries, ψ are constant. Though Eq. (10b) is elliptic, the requirement of vanishing vorticity outside the bound vortex sheets is kinematic. When flow becomes

supersonic, the governing equation for mean flow ψ need not change type.

Potential Function Solver. Previously, the classical Fast Fourier Transformation (FFT) technique was employed to solve the continuity equation for the potential function (Tan et al., 1984). This technique is numerically efficient because it reduces the three-dimensional problem to a set of two-dimensional Helmholtz equations in the Fourier domain. This technique works effectively for single vortex sheet design. However, due to the Gibbs phenomena near suction surface and pressure surface, the calculated blade mean wrap angle from Eq. (15b) in the current two-vortex-sheet design will oscillate. Besides, a uniform allocation in the pitchwise direction by FFT is not suitable for arbitrary tangential thickness specification. Hence, the continuity equation is discretized in all three directions and solved in the conservative form. This increases the program memory as well as CPU time substantially.

A standard 3-D Galerkin finite element method is used to solve the continuity equation. The boundary conditions applied to Eq. (11) are as follows. At the inflow boundary, the potential function is set to zero to give a uniform upstream flow assumption. Along the hub, shroud, blade suction, and blade pressure surfaces, the flow-tangency condition is imposed. For the periodic boundary (i.e., from inlet to blade leading edge and from blade trailing edge to outlet), the velocity should be continuous. At the outflow boundary, the Neumann boundary condition is used so the mass flux is set equal to the specified mass flow rate. Finally, along the periodic boundaries, the potential function is periodic (Dang, 1993); hence one more constraint should be imposed, i.e.,

$$\Phi(r, f, z) = \Phi(r, f + \frac{2\pi}{B}, z) \tag{16a}$$

The same boundary condition was found to apply between blade suction and blade pressure surfaces. If one takes an annular path wrap around the blade row, from Kelvin theorem the specified circulation is contributed solely by the flow from the blade passage ($f_s \le \theta \le f_p + 2\pi/n$). The circulation inside the blade should be zero ($f_p \le \theta \le f_s$). Thus, the tangential velocity inside the blade should vanish, which means

$$\Phi(r, f_s, z) = \Phi(r, f_p + 2\pi/n, z) \tag{16b}$$

This boundary condition imposed by Eq. (16b) is consistent with the specified mean swirl distribution defined in Eq. (1b).

Hyperbolic Equation Solver. The governing equation for the blade mean wrap angle $\bar{f}$, Eq. (15b), is hyperbolic. A finite element-based upwind scheme is developed to integrate the blade wrap angle (Yang et al., 1993). The solution for Eq. (15b) requires the specification of an integration constant for $\bar{f}$, which is called the "stacking condition" (Tan et al., 1984). The specified blade wrap stacking value must be a line from hub to shroud and not coincide with any of the streamlines. The specification of the blade stacking condition, just like the mean swirl distribution, gives an useful control on blade shape as well as flow field (Yang et al., 1993).

Grid Generation. During the iteration process for the blade profile, the grid distributions in the blade-to-blade planes and periodic boundaries change at every iteration level. To reduce the grid-generation task, an **H**-grid topology is employed. To impose the boundary conditions of Eq. (16a) and (16b) conveniently, the grid in the meridional plane (r, z) is always fixed. Only a stretching function in the pitchwise direction θ is used to generate a three-dimensional grid distribution during iterations. In the present study, the grid distribution in the pitchwise direction is equally spaced. Also, the grid system used in the Euler analysis is the direct outcome of the inverse design.

MEAN SWIRL DISTRIBUTION $r\bar{V}_\theta$ AND SPLITTING FUNCTION t

Specification of $r\bar{V}_\theta$ distribution. The swirl distribution $r\bar{V}_\theta$ cannot be specified arbitrarily (Tan et al., 1984; Hawthorne and Tan, 1987; Yang et al., 1993). The Kutta condition at the blade trailing edge requires the streamwise derivative of the mean swirl value to be zero (Tan et al. 1984). Additionally, if one assumes a zero incidence at the blade leading edge, the streamwise derivative of mean swirl value should vanish at the leading edge also. For the blade upstream and downstream regions, a constant value of mean swirl is imposed for a free vortex design. Hence, a distribution of "loading" (streamwise derivative of the mean swirl) is prescribed to control the swirl distribution from leading edge to trailing edge in the present study. It is observed that "loading" distributions that depart greatly from a linear distribution along streamlines may result in peculiarly shaped airfoils having undesirable mechanical and/or aerodynamic properties. Thus, a smooth variation of the mean swirl distribution is desirable.

Independence of splitting function t. The splitting function $t(r, z)$ is used to separate the mean swirl distribution into two fractions to give two different strengths of bound vortex sheets, i.e., one for suction surface and one for pressure surface. By using a different splitting function t, each vortex generates a different induced flow field. By expanding and rearranging the velocity from the sum of two bound vortex sheets in Eq.(7), we have

$$\begin{aligned} &-S(\alpha_s)\nabla(tr\bar{V}_\theta) - S(\alpha_p)\nabla((1-t)r\bar{V}_\theta) = \\ &-\left\{tS(\alpha_s) + (1-t)S(\alpha_p)\right\}\nabla r\bar{V}_\theta - r\bar{V}_\theta\left\{S(\alpha_s) - S(\alpha_p)\right\}\nabla t \end{aligned} \tag{17a}$$

and can note that

$$tS(\alpha_s) + (1-t)S(\alpha_p) = \frac{1}{2}S(\alpha_s) + \frac{1}{2}S(\alpha_p) + T_1 \tag{18}$$

and

$$S(\alpha_s) - S(\alpha_p) = T_2 \tag{19}$$

where T_1 (see Fig. 2d) and T_2 (see Fig. 2e) are periodic step functions, defined as

$$T_t = \begin{cases} (t - \frac{1}{2})\Delta f & \text{blade-to-blade} \\ -(2t-1)\frac{\pi}{n} + (t - \frac{1}{2})\Delta f & \text{within the blade} \end{cases}$$

and

$$T_2 = \begin{cases} \Delta f & \text{blade - to - blade} \\ -\dfrac{2\pi}{n} + \Delta f & \text{within the blade} \end{cases}$$

Thus, the velocity in the blade-to-blade plane from the sum of two bound vortex sheets in Eq.(17a) is equivalent to

$$-S(\alpha_1)\nabla(r\bar{V}_\theta) - S(\alpha_2)\nabla((1-t)r\bar{V}_\theta) = \\ -S(\alpha_1)\nabla\left(\frac{1}{2}r\bar{V}_\theta\right) - S(\alpha_2)\nabla\left(\frac{1}{2}r\bar{V}_\theta\right) - \left\{(t-\frac{1}{2})\Delta f\nabla r\bar{V}_\theta + \Delta f r\bar{V}_\theta\nabla t\right\} \quad (17b)$$

It is clear that the last term on the RHS of Eq. (17b) is a mean flow distribution, i.e., without tangential variation. In other words, a different splitting function t does not change the slope of the sawtooth part (compare Fig. 2b with Fig. 2c) but only raises or lowers the mean flow level. A different splitting function t changes the source term of the Stokes stream function ψ in Eq. (10b) and alters the mean flow level to give an equivalent amount of meridional velocity, so that the tangential vorticity outside the two bound vortex sheets vanishes. From the mass flow conservation, the potential part will adjust itself based on its mean flow level from the Stokes stream function and the sawtooth part and leave the blade circulation unchanged. Thus, the solution is determined by mean swirl distribution $r\bar{V}_\theta$ and blade tangential thickness Δf uniquely.

EULER CODE DESCRIPTION

The program used to analyze the designed blade rows and compare them with results from the inverse design was a three-dimensional Euler code. The codes used here have been reported by Jameson et al. (1981). This cell-centered finite volume program uses a 4-stage Runge-Kutta integration procedure to march the solution to a steady state. The Rieman upstream boundary condition is imposed. Radial equilibrium is assumed at the outlet, with downstream pressure adjusted to match the specified mass flow rate. At the hub, pressure, suction and shroud surfaces, an extrapolated normal pressure gradient boundary condition is employed in conjunction with an adiabatic wall. No tip leakage flow is employed. A second order artificial viscosity is used to capture shocks, and a fourth order artificial viscosity is implemented to avoid numerical oscillation. The expression of artificial fluxes in ξ-direction is

$$\begin{aligned} AV = {} & \frac{\nu_2}{2}\left[\left(S_2\frac{V}{\Delta t}\right)_{i,j,k} + \left(S_2\frac{V}{\Delta t}\right)_{i+1,j,k}\right](U_{i+1,j,k} - U_{i,j,k}) \\ & - \frac{\nu_2}{2}\left[\left(S_2\frac{V}{\Delta t}\right)_{i-1,j,k} + \left(S_2\frac{V}{\Delta t}\right)_{i,j,k}\right](U_{i,j,k} - U_{i-1,j,k}) \\ & + \frac{\nu_4}{2}\left[\left(\frac{V}{\Delta t}\right)_{i,j,k} + \left(\frac{V}{\Delta t}\right)_{i+1,j,k}\right](U_{i+2,j,k} - 3U_{i+1,j,k} + 3U_{i,j,k} - U_{i-1,j,k}) \\ & - \frac{\nu_4}{2}\left[\left(\frac{V}{\Delta t}\right)_{i-1,j,k} + \left(\frac{V}{\Delta t}\right)_{i,j,k}\right](U_{i+1,j,k} - 3U_{i,j,k} + 3U_{i-1,j,k} - U_{i-2,j,k}) \end{aligned} \quad (20)$$

where U is the state variable, ν_2 and ν_4 are second and fourth order artificial viscosity coefficients, in the present study $\nu_2 = 0.1$ and $\nu_4 = 0.02$ are used. V is the cell volume, Δt is the integration time step from Fourier analysis, and S_ξ is the pressure switch defined by $|p_{i-1,j,k} - 2p_{i,j,k} + p_{i-1,j,k}|/p_{i,j,k}$. A similar expression of artificial fluxes is used in the η-direction and ζ-direction.

RESULTS AND DISCUSSION

Design of a single stage of compressor is used to demonstrate the current inverse design technique. The design input list is summarized in Table 1. First, the subsonic stator design will be examined to illustrate the independence on the calculated blade mean wrap angle by using suction side and pressure side boundary conditions. Next, the transonic rotor design is used to demonstrate the application of the current inverse technique in transonic flow.

TABLE 1 Compressor design input

Design Weight Flow	6 kg/s
Specific Flow	179.3 kg/s-m^2
Isentropic pressure ratio	1.556
Rotor tip diameter	0.131 m
Rotor Hub/Tip radius ratio	0.642
Number of rotor blades	23
Rotor tip inlet Mach number	1.23
Rotor meridional mesh	Fig. 9(a)
Rotor mean swirl distribution	Fig. 9(b)
Rotor blade tangential thickness	Fig. 9(c)
Stator tip diameter	0.132 m
Stator Hub/Tip radius ratio	0.696
Number of stator blades	49
Stator hub inlet Mach number	0.6
Stator meridional mesh	Fig. 3(a)
Stator mean swirl distribution	Fig. 3(b)
Stator blade tangential thickness	Fig. 3(c)

Figure 3a shows the specified hub and shroud profiles with grid distribution in the meridional plane for stator. All dimensions are normalized to the blade tip radius. The employed grid has 71x41 nodes in the meridional plane (43 nodes are used from the leading edge to the trailing edge) and 27 nodes in the circumferential direction. The prescribed mean swirl distribution is shown in Fig. 3b where the velocity is normalized by inlet total temperature (i.e., $\sqrt{RT_t}$). The specified blade tangential thickness distribution Δf is shown in Fig. 3c. The location of maximum blade tangential thickness is at 30% and 33% of axial chord for hub and tip sections, respectively. The blade is stacked at 67% of axial chord. A fully converged solution (change in blade mean wrap angle less than 10^{-7} rad., see Fig. 4) for this grid requires on the order of four hours of CPU time on a PC (Pentium-Pro 200). The number of iterations using blade suction side boundary condition is 68; while using pressure side boundary condition is 69. The blade shapes using the two boundary conditions are nearly identical; the difference is shown in Fig. 5a. The maximum difference in the derived profile is 0.00136 rad. (0.86% of its local blade mean wrap angle) near the leading edge at the hub. Figure 5b illustrates the calculated two blade profiles at hub. A 3-D view of the designed stator blades is shown in Fig. 5c. Using the 3-D blade shape from the inverse

design, an Euler calculation was performed to compare the flow field from these two different schemes. A detailed comparison of these two solutions is made by the cross section plots of Mach number at the leading edge, mid-passage, and the trailing edge of passage (Fig. 6a-6c). In addition, the Mach number at the hub in the blade-to-blade plane is given in Fig. 7. From these plots, the agreement between these two is good except near the leading edge at the hub where the solution from Euler calculation shows a higher Mach number of 0.72 than 0.68 from inverse design. The incidence angle computed from Euler analysis seems to be slightly higher than the designed value at hub. Finally, the blade-to-blade averaged swirl from Euler analysis is given in Fig. 8. The calculated mean swirl distribution from a direct Euler analysis is closely matched with the prescribed one as indicated in Fig. 3b.

Figure 9a shows the computational grid in the meridional plane for rotor. The employed grid has 71x37 nodes in the meridional plane (41 nodes is used from the leading edge to the trailing edge) and 31 nodes in the circumferential direction. The prescribed mean swirl distribution is shown in Fig. 9b. The specified blade tangential thickness distribution Δf is shown in Fig. 9c. The location of maximum blade tangential thickness is at 17% and 50% of axial chord for hub and lip sections, respectively. The blade is stacked at 85% of axial chord. A 3-D view of the designed rotor blades is shown in Fig. 10. By using the 3-D blade shape from inverse design, a Euler calculation is performed to compare the flow field from these two different schemes in transonic flow. A detailed comparison of these two solutions is made by the cross section plots of Mach number at 0, 18, 50, 82, and 100% of passage (Fig. 11a-11e). In addition, the Mach number at the tip in the blade-to-blade plane is given in Fig. 12. From these plots, the solutions between these two is only similar. The solutions near the tip, i.e., region of high Mach number, show quite different results after the shocks. The solution from the inverse design gives a much higher Mach number after the shocks. Finally, the blade-to-blade averaged swirl from Euler analysis is given in Fig. 13. Clearly, the calculated mean swirl distribution from a direct Euler analysis shows a higher compression at the tip than the prescribed one as plotted in Fig. 9b. A further investigation of the results from Euler analysis on the entropy increment after the shocks is given in Fig. 14. The change of entropy is significant. At the trailing edge, 50% of the passage is nonisentropic. The generation of vorticity after the shocks is shown in Fig. 15. Obviously, the flow on the pressure surface near the tip becomes rotational. A modification of the present inverse formulation to account for entropy change and generation of vorticity is required.

CONCLUSIONS

A new formulation of three-dimensional inverse design method for arbitrary blade thickness has been developed, in which the blade suction surface and pressure surface, are represented by two periodic bound vortex sheets. By using a splitting function f, blade passage mean swirl distribution is split into two fractions to formulate two bound vortex sheets. The strength of each bound vortex sheet is related to its blade wrap and its mean swirl change. A different splitting function f gives a different induced flow field by each single bound vortex sheet, but the sum of the sawtooth part of two bound vortex sheets is different by a constant. The present inverse design scheme is uniquely determined by the specification of mean swirl distribution and blade tangential thickness.

The generalized blade surface formulation, Eq. (2), provides a convenient way to handle large blade turning as well as large blade thickness. The difficulty of the Gibbs phenomena is avoided and a precise blade surface velocity is obtained by implementing an analytical sawtooth function. Thus, the present inverse design method can deal with blade thickness quite arbitrarily. However, for a blade with blunt leading and trailing edges an O-grid-mesh is recommended. A change of grid topology is reserved for future work.

By using the Jameson's upwinding density proposed by Holst and Ballhaus (1979), a stable supersonic calculation is obtained for inverse design problems. A normalized projection of upstream density equation from three grid directions is proposed, i.e., Eq.(15). No coordinate transformation is required to compute the retarding density. However, comparison between the prescribed mean swirl distribution and the calculated mean swirl distribution shows a large difference at the rotor tip.

The current isentropic and irrotational assumptions are not correct for a strong shock design. Klopfer and Nixon (1984) have introduced a non-isentropic formulation that greatly improves the accuracy of the continuity equation when stronger shocks occur. By assuming the adiabatic condition, changes in entropy across the shock can be incorporated in Eq. (14) to become

$$\frac{\rho}{\rho_\infty} = \left\{ \frac{1 + 0.5\omega^2 r^2 - 0.5W^2}{C_p T_\infty} \right\}^{\frac{1}{\gamma - 1}} \times e^{-\Delta S / R} \qquad (21)$$

where the changes in entropy ΔS are obtained from normal shock relations directly. A modification of the current technique to deal with entropy change and generation of vorticity is reserved for future work.

ACKNOWLEDGMENTS

The author would like to thank Dr. Choon S. Tan and Prof. Sir William R. Hawthorne of the Gas Turbine Laboratory at Massachusetts Institute of Technology for suggesting the original idea of the two vortex sheets inverse design method to treat the blade thickness problem. The research was partially supported by the Chung-Shan Institute of Science and Technology of the Republic of China under Contract CS 84-0201-D-216-001.

REFERENCES

Hawthorne, W. R., Wang, C., Tan, C. S., and McCune, J. E., 1984. "Theory of Blade Design for Large Deflections: Part I—Two-Dimensional Cascade," ASME *Journal of Engineering for Gas Turbines and Power*, Vol. 106, pp. 346-353.

Tan, C. S., Hawthorne, McCune, J. E., and Wang, C., 1984. "Theory of Blade Design for Large Deflections: Part II—Annular Cascades," ASME *Journal of Engineering for Gas Turbines and Power*, Vol. 106, pp. 354-365.

Lamb, H., 1932, *Hydrodynamics*, 6th ed. Dover Publications, New York.

Lighthill, M. J., 1958, "Fourier Analysis and Generalized Functions," Cambridge University Press, United Kingdom.

Hawthorne, W. R., and Tan, C. S., 1987, "Design of Turbomachinery Blading in 3-D Flow by the Circulation Method: A Progress Report," ICIDES-II, pp. 207-226.

Ghaly, W. S., 1990, "A Parametric Study of Radial Turbomachinery Blade Design in Three-Dimensional Subsonic Flow," ASME *Journal of Turbomachinery*, Vol. 112, pp. 338-345.

Borges, J. E., 1990a, "A Three-Dimensional Inverse Method in Turbomachinery: Part I—Theory," ASME *Journal of Turbomachinery*, Vol. 112, pp. 364-354.

Borges, J. E., 1990b, "A Three-Dimensional Inverse Method in Turbomachinery: Part II—Experimental Verification," ASME *Journal of Turbomachinery*, Vol. 112, pp. 355-361.

Zangeneh, M., 1990, "Three Dimensional Design of a High Speed Radial-Inflow Turbine by a Novel Design Method," ASME Paper No. 90-GT-235.

Zangeneh, M., 1991, "A Compressible Three Dimensional Blade Design Method for Radial and Mixed Flow Turbomachinery Blades," *Int. J. Numerical Methods in Fluids*, Vol. 13, pp. 599-624.

Dang, T. Q., 1993, "A Fully Three-Dimensional Inverse Method for Turbomachinery Blading in Transonic Flows," ASME *Journal of Turbomachinery*, Vol. 115, pp. 354-361.

Yang, Y. L., Tan, C. S., and Hawthorne, W. R., 1993, "Aerodynamic Design of Turbomachinery Blading in Three-Dimensional Flow: An Application to Radial Inflow Turbines," ASME *Journal of Turbomachinery*, Vol. 115, pp. 602-613.

Zangeneh, M., 1994, "Inviscid/Viscous Interaction Method for Three-Dimensional Inverse Design of Centrifugal Impeller," ASME *Journal of Turbomachinery*, Vol. 116, pp. 280-290.

Dang, T. Q., and Isgro, I., 1995, "Euler-Based Inverse Method for Turbomachine Blades Part I: Two-Dimensional Cascades," AIAA J., Vol. 33, No. 12, pp. 2309-2315

Tjokroaminata, W. D., Tan, C. S., and Hawthorne, W. R., 1996, "A Design Study of Radial Inflow Turbines with Splitter Blades in Three-Dimensional Flow," ASME *Journal of Turbomachinery*, Vol. 118, pp. 353-361.

Zangeneh, M., 1996, "Inverse Design of Centrifugal Compressor Vaned Diffusers in Inlet Shear Flows," ASME *Journal of Turbomachinery*, Vol. 118, pp. 385-393.

Jameson, A., Schmidt, W., and Turkel, E., 1981, "Numerical Solutions of the Euler Equations by Finite Volume Methods Using Runge-Kutta Time-Stepping Schemes," AIAA Paper No. 81-1259.

Jameson, A., 1975, "Transonic Potential Flow Calculations Using Conservative Form," AIAA *Second Computational Fluid Dynamics Conference Proceedings*, June, 1975, pp. 148-155.

Holst, T. L., and Ballhaus, W., 1979, "Fast, Conservative Schemes for the Full Potential Equation Applied to Transonic Flows," AIAA Journal, Vol. 17, Feb., 1979, pp. 145-152.

Klopfer, G. H. and Nixon, D., 1984, "Nonisentropic Potential Formulation for Transonic Flows," AIAA Journal, Vol. 22, pp. 770-776.

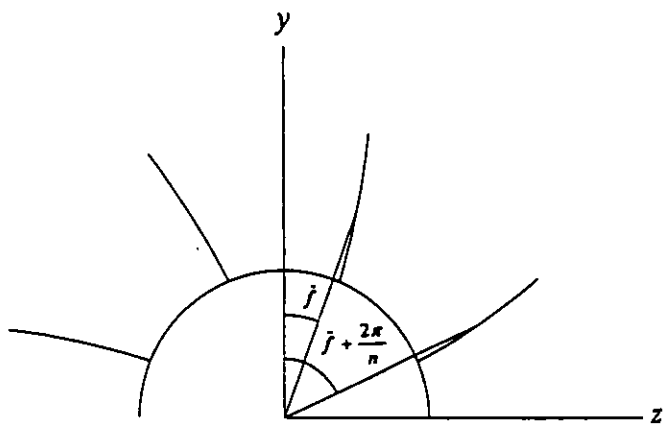

Fig.. 1(a) Definition of blade wrap angle by single vortex sheet (Tan. et al., 1984)

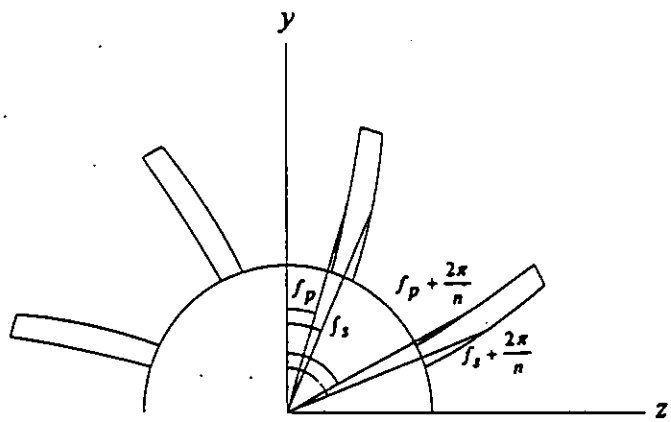

Fig. 1(b) Definition of blade wrap angle by two periodic vortex sheets

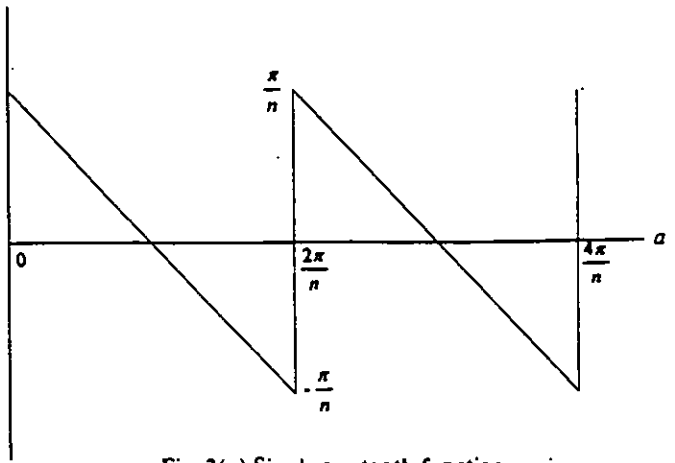

Fig. 2(a) Single sawtooth function

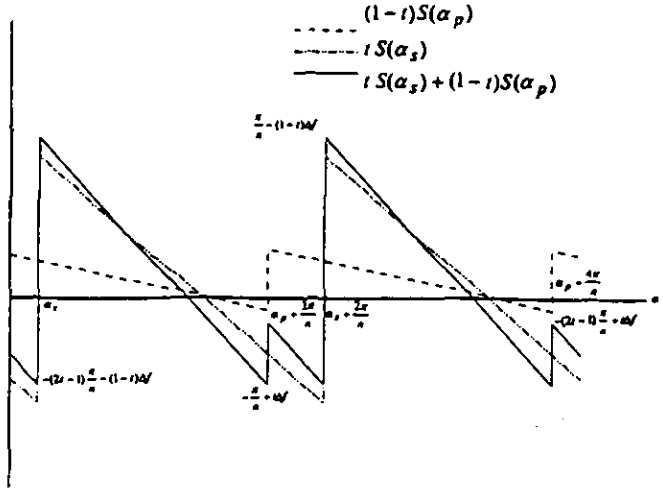

Fig. 2(b) Two sawtooth functions with different strength

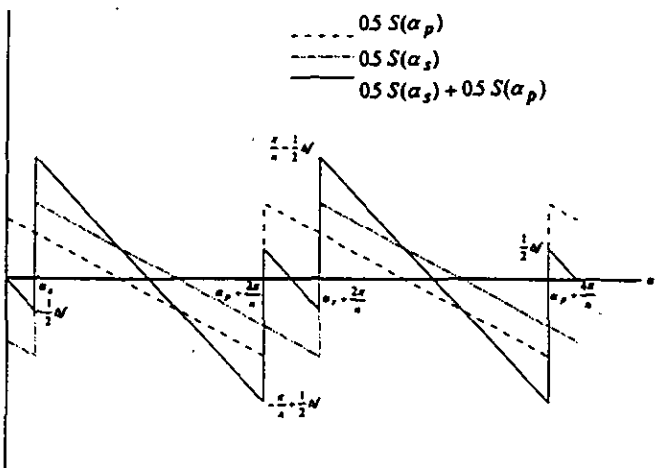

Fig. 2(c) Two sawtooth function with equal strength, $t = 0.5$

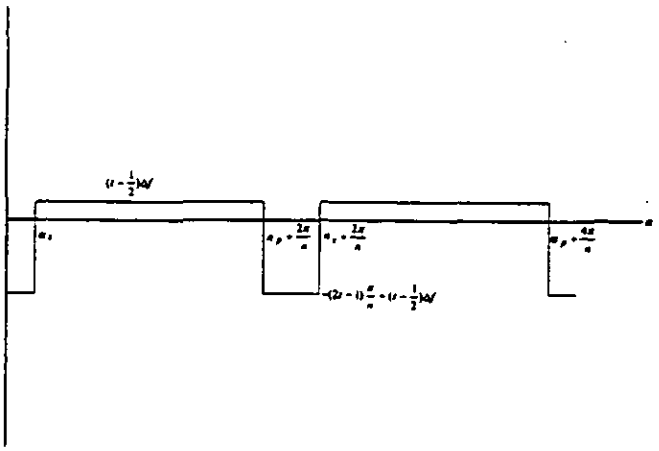

Fig. 2(d) Periodic step function T_1

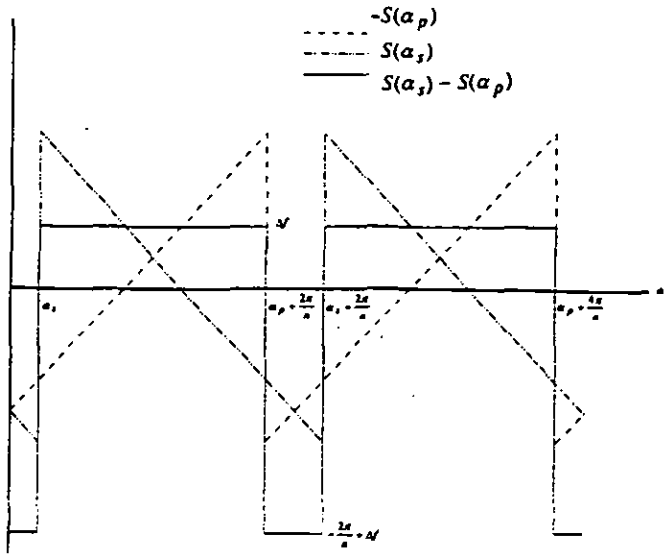

Fig. 2(e) Periodic step function T_2

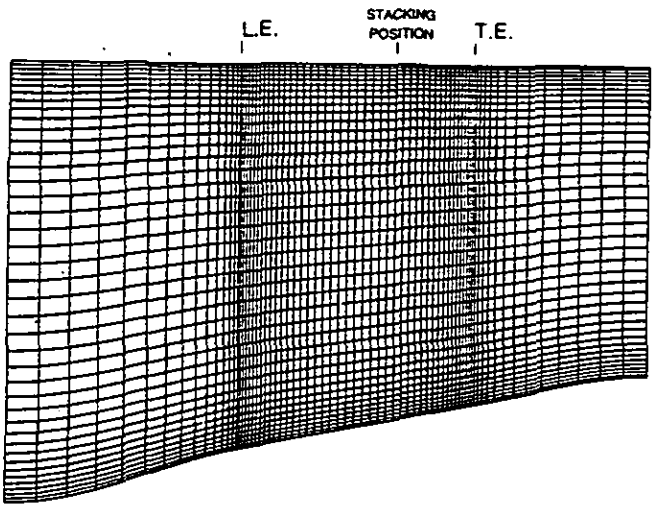

Fig. 3(a) Computational grid in the meridional plane for stator

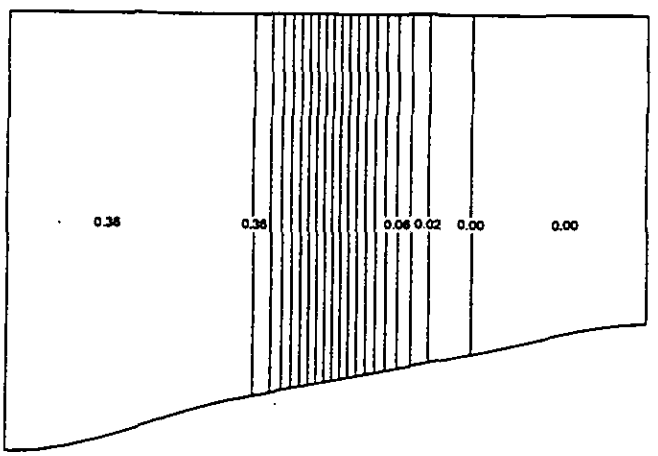

Fig. 3(b) Contour of specified mean swirl distribution for stator (contour increment 0.02)

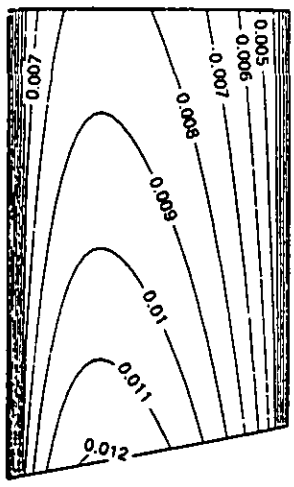

Fig. 3(c) Contour of specified blade tangential thickness Δf for stator (Contour increment 0.001 rad.)

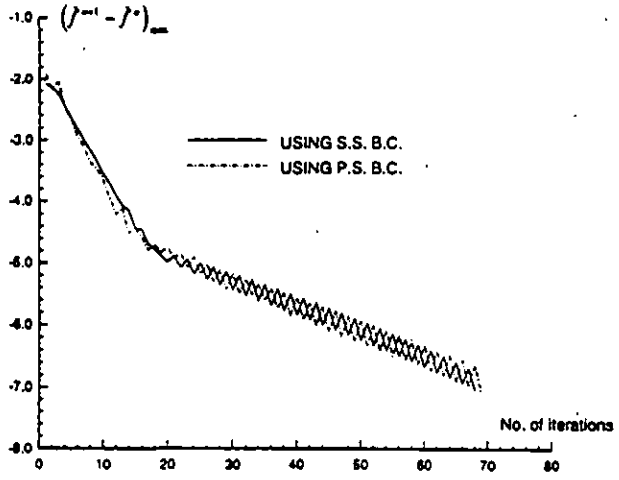

Fig. 4 Iteration histories by using blade suction side boundary condition and pressure side boundary condition

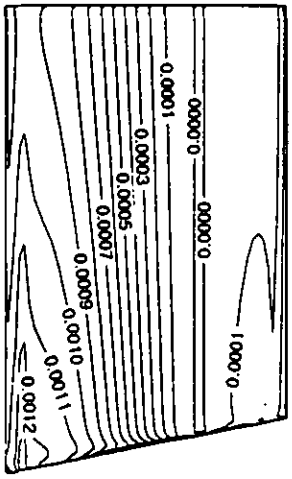

Fig. 5(a) Difference in calculated blade mean wrap angle by using blade suction side and using pressure side boundary condition (contour increment 0.0001 rad.)

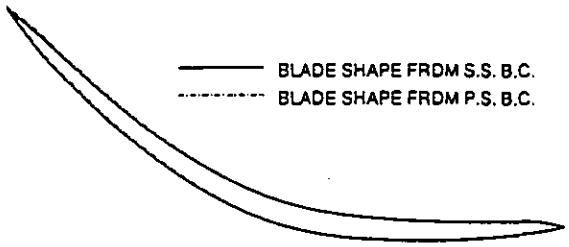

Fig. 5(b) Calculated blade shape at hub

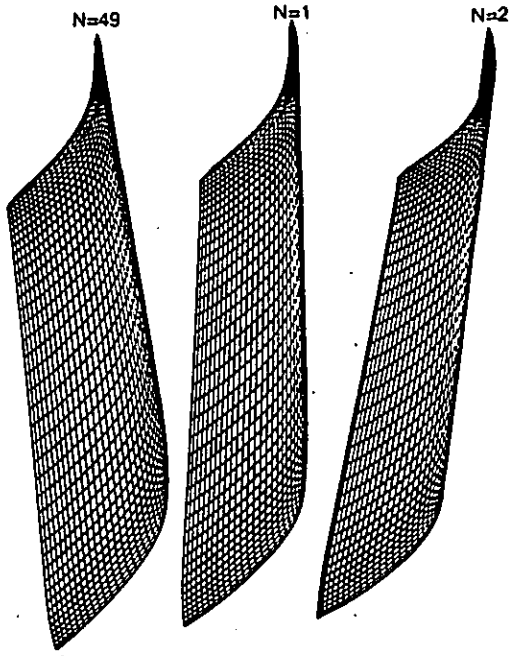

Fig. 5(c) Solid modeling of calculated stator blade shape

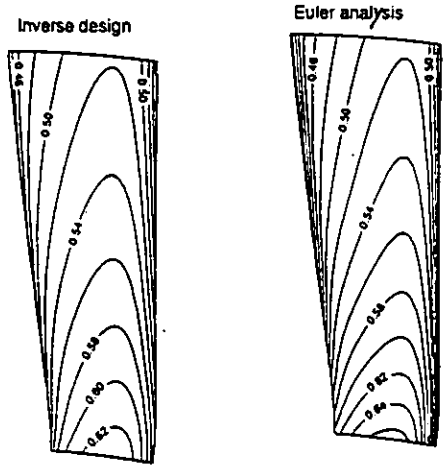

Fig. 6(a) Mach number at the leading edge (contour increment 0.02)

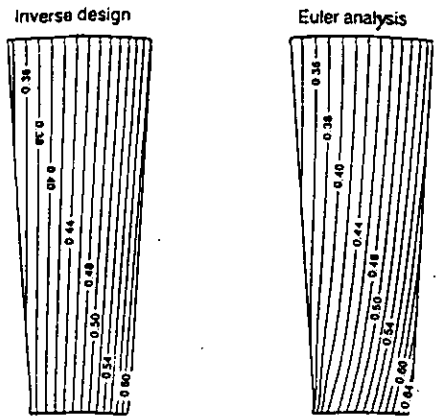

Fig. 6(b) Mach number at mid-passage (contour increment 0.02)

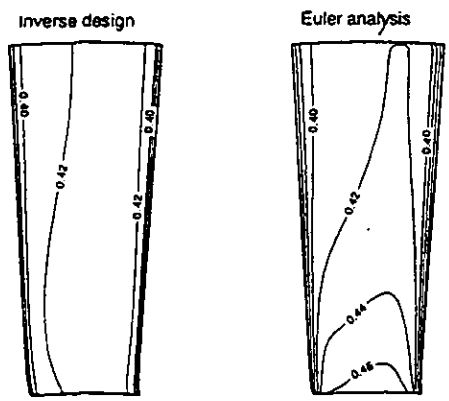

Fig. 6(c) Mach number at the trailing edge (contour increment 0.02)

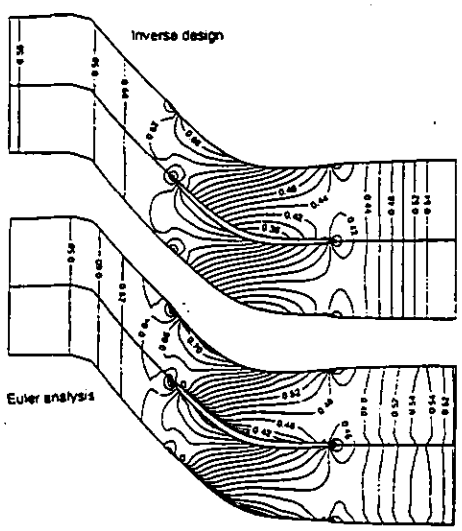

Fig. 7 Mach number at the hub (contour increment 0.02)

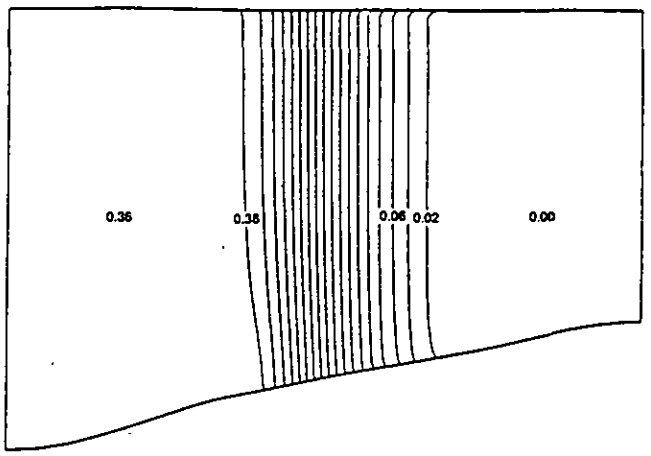

Fig. 8 Contour of calculated mean swirl distribution from Euler solver (contour increment 0.02)

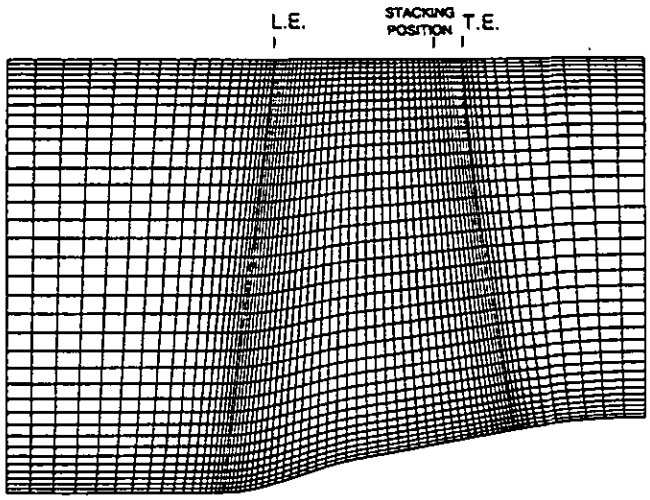

Fig. 9(a) Computational grid in the meridional plane for rotor

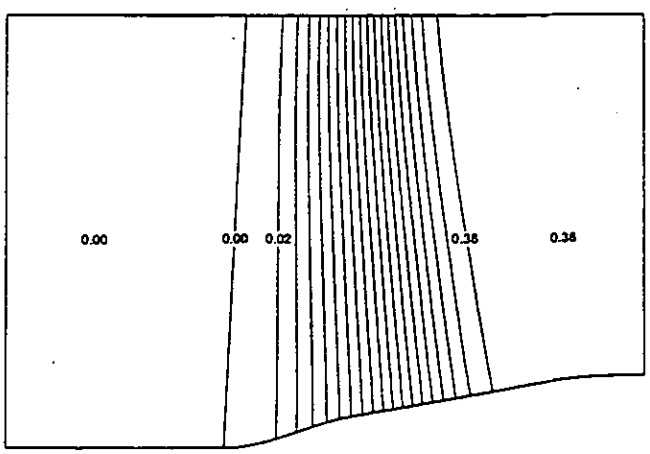

Fig. 9(b) Contour of specified mean swirl distribution for rotor (contour increment 0.02)

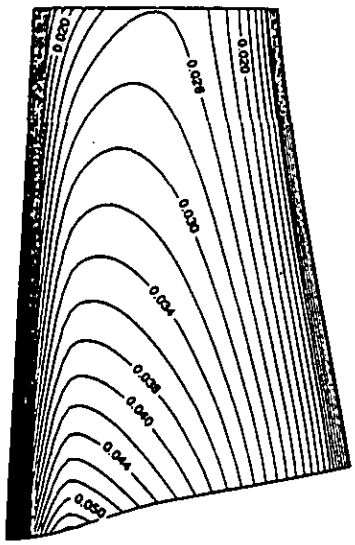

Fig. 9(c) Contour of specified blade tangential thickness Δf for rotor (Contour increment 0.002 rad.)

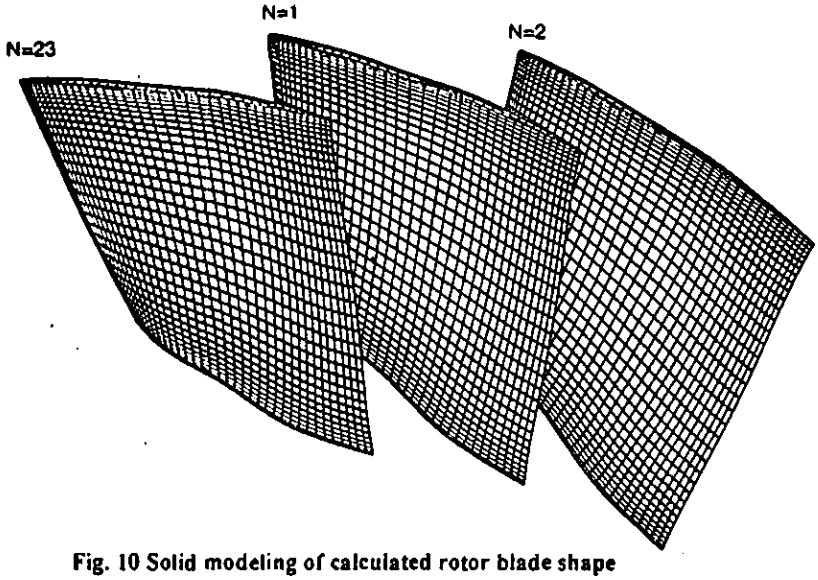

Fig. 10 Solid modeling of calculated rotor blade shape

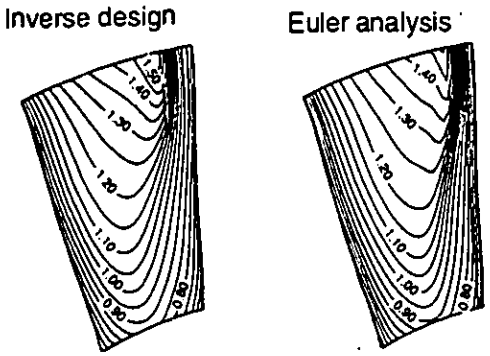

Fig. 11(a) Mach number at the leading edge (contour increment 0.05)

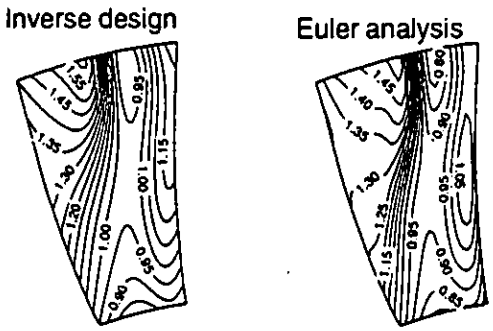

Fig. 11(b) Mach number at 18% passage (contour increment 0.05)

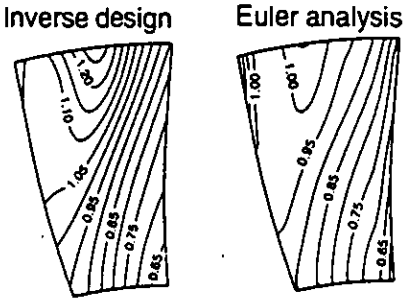

Fig. 11(c) Mach number at mid-passage (contour increment 0.05)

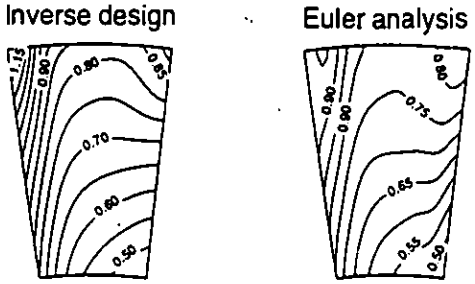

Fig. 11(d) Mach number at 82% passage (contour increment 0.05)

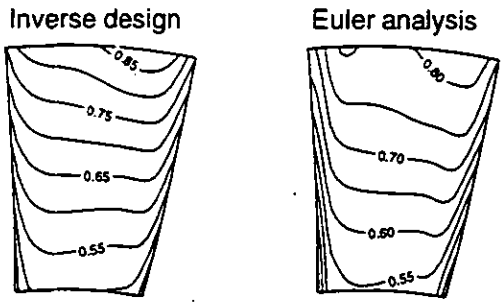

Fig. 11(e) Mach number at the trailing edge (contour increment 0.05)

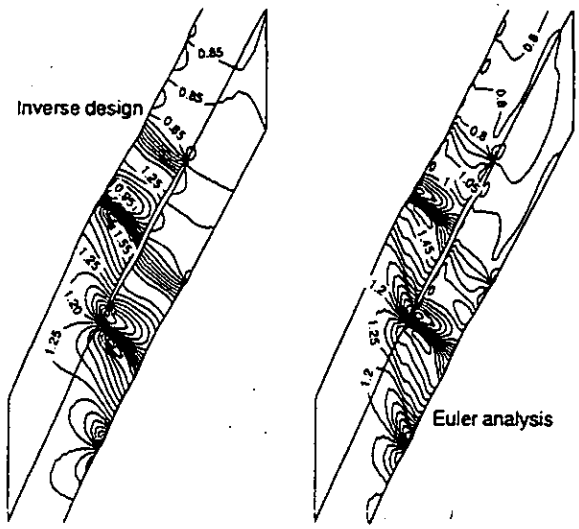

Fig. 12 Mach number at the tip (contour increment 0.05)

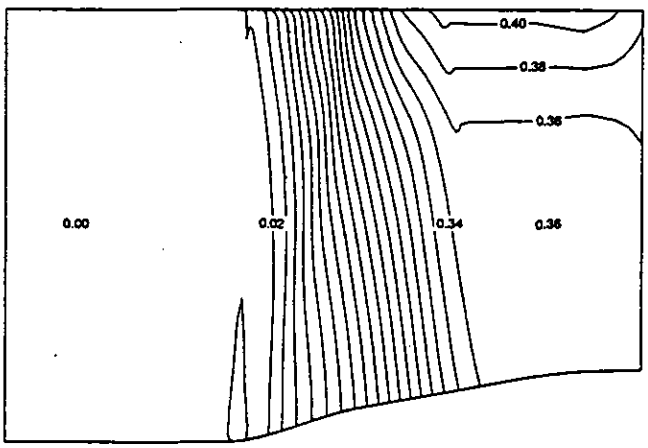

Fig. 13 Contour of calculated mean swirl distribution from Euler solver (contour increment 0.02)

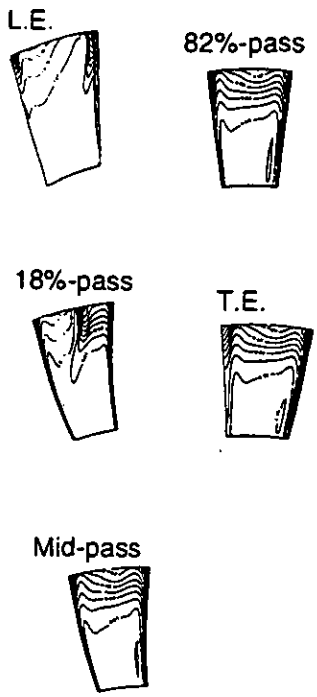

Fig. 14 Contour of calculated entropy $\Delta s/R$ from Euler analysis (contour increment 0.01)

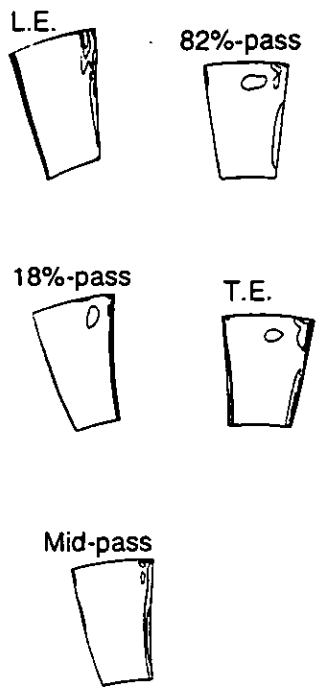

Fig. 15 Contour of calculated magnitude of vorticity $|\bar{\Omega}|$ from Euler analysis